What Drives Negative K_{DP} above the Melting Layer? The Hidden Role of Secondary Ice Production

Yongjie Huang[1,3], Greg M. McFarquhar[2,3], Alexander V. Ryzhkov[2,4], Ming Xue[1,3], Dhwanit J. Mise[1,2,3], Jeffrey Snyder[4], Lulin Xue[5], William Y.Y. Cheng[5], Mariko Oue[6], Pavlos Kollias[6,7], Michael P. Jensen[7], Timothy Logan[8], Eric Bruning[9]

[1]Center for Analysis and Prediction of Storms, University of Oklahoma, Norman, OK, USA
[2]Cooperative Institute for Severe and High-Impact Weather Research and Operations, University of Oklahoma, Norman, OK, USA
[3]School of Meteorology, University of Oklahoma, Norman, OK, USA
[4]NOAA/OAR National Severe Storms Laboratory, Norman, OK, USA
[5]NSF National Center for Atmospheric Research, Boulder, CO, USA
[6]Division of Atmospheric Sciences, Stony Brook University, Stony Brook, NY, USA
[7]Brookhaven National Laboratory, Upton, NY, USA
[8]Texas A&M University, College Station, TX, USA
[9]Texas Tech University, Lubbock, TX, USA

Key Points:

- Negative K_{DP} regions above the melting layer in deep convection are frequently detected by both C- and S-band radars.
- Negative K_{DP} is linked to lightning and likely reflects electrically aligned ice particles in deep convection.
- Simulated negative K_{DP} occurs primarily when secondary ice production, especially fragmentation of freezing drops, is included.

Corresponding author: Yongjie Huang, Yongjie.Huang@ou.edu; huangynj@gmail.com

Abstract

Secondary ice production (SIP) remains a major uncertainty in understanding deep convection because its rates and controlling conditions are poorly constrained. Using the Tracking Aerosol Convection Interactions Experiment (TRACER) C-band and operational S-band radar observations, Houston Lightning Mapping Array (HLMA) lightning data, and large-eddy simulations (LESs), this study investigates negative K_{DP} observed above the melting layer as a potential signature of SIP and storm electrification. Among 413 observed deep convective cells, 238 cases ($\sim$57.6%) exhibit negative K_{DP} above the melting layer, and 49 of 123 lightning-active cases ($\sim$39.8%) show negative K_{DP} near HLMA sources. These observations suggest that negative K_{DP} is associated with small, vertically oriented, electrically aligned ice particles. LESs with spectral bin microphysics reproduce negative K_{DP} with high likelihood only when SIP is included, especially fragmentation of freezing drops, which increases ice water path, decreases liquid water path, and reduces accumulated precipitation by $\sim$7.6% in the examined case.

Plain Language Summary

Thunderstorms contain many small ice particles that influence lightning, rainfall, and how storms grow, but scientists still do not know exactly how these particles form in natural clouds. This study uses radar and lightning observations from the 2022 TRACER field campaign near Houston, Texas, together with high-resolution storm simulations, to examine a radar signature that may reveal these ice particles. The study found that many isolated deep convective clouds exhibited an unusual radar signature, called negative K_{DP}, above the melting layer, where ice particles are present. These signals were detected by both research and operational weather radars, and some occurred near lightning activity. This suggests that the signals may be caused by small ice particles that become vertically aligned by electric fields inside thunderstorms. Simulations showed that this radar signature is reproduced mainly when ice multiplication processes are included, especially when freezing drops break apart. This process increases ice, reduces liquid water, and decreases accumulated rainfall by about 7.6% in the examined case. These results help clarify how ice production, storm electrification, and precipitation are connected in deep convection.

1 Introduction

Specific differential phase, K_{DP}, is a polarimetric radar variable that describes the range derivative of differential propagation phase, Φ_{DP}, between horizontally and vertically polarized radar waves. In rain and in many populations of horizontally oriented anisotropic ice particles, K_{DP} is typically positive because horizontally polarized waves experience a larger phase shift than vertically polarized waves (Ryzhkov & Zrnić, 2019). Negative K_{DP}, particularly above the melting layer, is therefore an unusual and physically informative signature. It has commonly been interpreted as evidence that anisotropic ice particles have been rotated from their preferred aerodynamic, near-horizontal orientation toward a more vertical orientation by strong storm electric fields (Caylor & Chandrasekar, 1996; Zrnic & Ryzhkov, 1999; Ryzhkov & Zrnić, 2007; Weber et al., 2024). Because such electric fields develop during thunderstorm electrification, negative K_{DP} above the melting layer provides a potentially valuable radar-based indicator of ice particle alignment, charge structure, and lightning initiation processes.

Early polarimetric radar studies demonstrated that the orientation of ice particles in thunderstorms can change rapidly in response to evolving electric fields, with the particles likely consisting of needle-shaped ice crystals. For example, Metcalf (1995) showed that hydrometeor reorientation associated with thunderstorm electrification could be observed using S-band polarimetric radar. Caylor and Chandrasekar (1996), using Florida Convection and Precipitation Electrification project (CaPE) observations, further linked decreases in K_{DP} prior to lightning and rapid recovery after lightning to the electrical alignment and relaxation of ice crystals. Their observations suggested that negative K_{DP} values, often on the order of -0.3 to -0.5° km^{-1}, could develop in cloud-top ice regions several kilometers above the 0°C level. Subsequent studies expanded this phenomenology across different storm environments, radar wavelengths, and lightning datasets (e.g., Figueras i Ventura et al., 2013; Mattos et al., 2016, 2017; Biggerstaff et al., 2017; Wang et al., 2024a, 2024b), showing that negative K_{DP} is not simply colocated with lightning, but may mark the development of strong electric fields and charge-layer boundaries that control where lightning initiates and propagates. For example, Mattos et al. (2016, 2017) showed that K_{DP} in the glaciated and upper mixed-phase regions became increasingly negative as lightning activity increased, and that negative K_{DP} developed before the first cloud-to-ground lightning in isolated compact thunderstorms. Biggerstaff et al. (2017) provided a more detailed electrical interpretation by showing that intracloud flashes in a Florida mesoscale convective system (MCS) initiated near the zero-K_{DP} boundary surrounding a negative-K_{DP} region, rather than within the negative-K_{DP} core itself. Wang et al. (2024a, 2024b) showed that composite K_{DP} in an isolated thunderstorm changed from positive to negative several minutes before the first intracloud flash, with the most negative cloud-top values occurring shortly before lightning initiation.

However, the microphysical interpretation of negative K_{DP} is not straightforward. A negative propagation phase signature does not require all particles in the radar sampling volume to be vertically oriented. Large dry aggregates and graupel often have small intrinsic K_{DP}, while contributing strongly to reflectivity. As a result, negative K_{DP} may arise from a mixed population in which small, anisotropic, electrically aligned ice crystals dominate the propagation phase, while larger graupel or aggregates dominate Z_H and partially mask the expected Z_{DR} signature (Hubbert et al., 2014). Large rimed particles are also central to noninductive charge separation and storm electrification through collisions with ice crystals in mixed-phase regions, whereas smaller anisotropic ice crystals may be the primary carriers of the negative K_{DP} propagation signal (Reynolds et al., 1957; Takahashi, 1978; Berdeklis & List, 2001; Saunders et al., 2006; Saunders, 2008). Thus, negative K_{DP} above the melting layer should be interpreted as an integrated signature of particle shape, size distribution, orientation, and electric-field strength rather than as a simple hydrometeor category. This raises a central unresolved question: what supplies the small anisotropic ice particles responsible for negative K_{DP} above the melting layer?

Secondary ice production (SIP) can substantially enhance ice particle number concentrations in mixed-phase clouds under appropriate thermodynamic and microphysical conditions, beyond what is predicted by primary ice nucleation alone (Field et al., 2017; Korolev & Leisner, 2020). Observational and modeling studies have shown that SIP processes can occur over a broader temperature range than the classic Hallett–Mossop mechanism (−3 to −8°C; Hallett & Mossop, 1974) and can substantially alter ice number concentrations in convective clouds, thereby influencing cloud evolution, cloud electrification, storm evolution, and surface precipitation (e.g., Lawson et al., 2015; Phillips et al., 2018, 2020; Huang et al., 2022; Lawson et al., 2022; Qu et al., 2022; Lawson et al., 2023; Korolev et al., 2024; Grzegorczyk, Wobrock, Canzi, et al., 2025a; Grzegorczyk, Wobrock, Dziduch, & Planche, 2025; Sun et al., 2025; Vongpaseut & Barthe, 2025). Huang et al. (2022) indicated that simulations including multiple SIP processes reproduced high-ice-water-content regions in tropical oceanic convective clouds across different temperature levels, with simulated ice number concentrations and radar reflectivity closely matching the observed magnitudes and vertical distributions. These results suggest that representing multiple SIP processes is important for improving numerical simulations of convective clouds. SIP processes therefore provide plausible pathways for replenishing the small ice particles that, once exposed to strong electric fields, may become vertically aligned and produce negative K_{DP}.

Recently, the second-generation C-band Scanning ARM (Atmospheric Radiation Measurement) Precipitation Radar (CSAPR2) observed more than 400 isolated deep convective cells under a wide range of environmental conditions during the Tracking Aerosol Convection Interactions Experiment (TRACER), conducted in the vicinity of Houston, Texas, in 2022 (Jensen et al., 2025; Huang, McFarquhar, Patil, et al., 2025; Mise et al., 2026); the National Science Foundation (NSF)-sponsored Experiment of Sea Breeze Convection, Aerosols, Precipitation, and Environment (ESCAPE; Kollias et al., 2025; Patil et al., 2026), a shorter-duration synergistic field campaign, overlapped with part of TRACER in the same region. An examination of these cells revealed frequent occurrences of negative K_{DP} regions located above the melting layer. We hypothesize that these negative K_{DP} signatures are caused by small, vertically oriented needle-like or columnar ice particles produced by SIP processes in mixed-phase regions and subsequently aligned with the in-cloud electric field. The hypothesis is tested by combining unique TRACER observations and large-eddy simulations (LESs) with the Weather Research and Forecasting (WRF) model. The scientific questions addressed in this study are as follows:

- To what extent can the WRF model reproduce regions of negative K_{DP} observed above the melting layer during TRACER, with and without SIP processes?
- Which specific SIP mechanism exerts the primary control on the formation of these negative K_{DP} signatures?
- How do SIP processes influence characteristics of convective clouds?

The remainder of the paper is organized as follows. Section 2 describes the TRACER observations and LES numerical experiments. Section 3 presents results from both observations and modeling. Section 4 summarizes the conclusions and discussion.

2 Data and Method

2.1 Observations

This study utilizes unique CSAPR2 radar observations collected during the TRACER Intensive Operational Period (IOP), conducted from June to September 2022, to examine negative K_{DP} signatures observed above the melting layer. CSAPR2 is a C-band, dual-polarization Doppler weather radar with a maximum range of 110 km and a range resolution of 100 m. During TRACER, CSAPR2 employed the Multisensor Agile Adaptive Sampling (MAAS) framework (Kollias et al., 2020) for real-time storm tracking. The CSAPR2 optimized convective cell tracking dataset (Oue et al., 2023), which includes Plan Position

Indicator (PPI) and Range Height Indicator (RHI) scans, provides a comprehensive collection of high-resolution radar observations of convective cells. In addition to CSAPR2 observations, data from the nearest operational Next-Generation Weather Radar (NEXRAD) S-band dual-polarization radar, KHGX, are used as supplementary observations. Through manual examination of both CSAPR2 and KHGX data, a total of 413 deep convective cells were identified for analysis (Mise et al., 2026). Houston Lightning Mapping Array (HLMA) flash-level data during ESCAPE (Logan et al., 2023; Bruning et al., 2024) are used to examine lightning activity associated with the deep convective cells.

2.2 Model Configuration

In this study, quasi-idealized LES simulations are conducted using the WRF model version 4.7.1 with a fast spectral bin microphysics (FSBM) scheme (Shpund et al., 2019) at a horizontal grid spacing of 250 m, which is the inner edge of horizontal grid spacings for convergence of convective vertical velocities (Jeevanjee, 2017). The horizontal domain size is 100 km $\times$ 100 km, and the model uses 81 vertical levels at a grid spacing of $\sim$250 m extending up to 20 km. The initial horizontally homogeneous thermodynamic environment is specified using hourly model-level fields from the European Centre for Medium-Range Weather Forecasts (ECMWF) Reanalysis v5 (ERA5) dataset (Hersbach et al., 2020), provided at a horizontal grid spacing of 0.25°. This dataset has been evaluated against all available TRACER IOP radiosonde soundings at the TRACER sites, with mean biases in temperature, relative humidity, and horizontal winds falling within the uncertainty ranges of the radiosonde sensors (Huang, McFarquhar, Patil, et al., 2025; Mise et al., 2026). Convection initiation adopts an updraft nudging method, as in our previous study (Huang et al., 2022).

In addition to the Hallett-Mossop (HM, or rime splintering) mechanism included in the original FSBM scheme, parameterizations of two additional SIP mechanisms, namely fragmentation of freezing drops (FFD, Phillips et al., 2018) and fragmentation during sublimation (SUBK, Deshmukh et al., 2022), are implemented. The hail option of the FSBM scheme is used, however, the scheme does not consider collisions between hail and other ice-phase hydrometeors. Moreover, large uncertainties remain in parameterizations of fragmentation during ice–ice collisions (Korolev & Leisner, 2020; Huang et al., 2022). Therefore, fragmentation during ice–ice collisions is not considered in this study, but it will be examined in future work.

To identify the location of dominant processes, especially SIP processes, responsible for producing negative K_{DP} regions, sensitivity experiments on SIP processes, including all three SIP processes off (SIPsOff), only one SIP process on (HMOn: only the Hallett-Mossop process on; FFDOn: only fragmentation of freezing drops on; SUBKOn: only fragmentation during sublimation), and all three SIP processes on (SIPsOn), are performed. In order to compare directly with the TRACER CSAPR2 observations, dual-polarization radar variables in each simulation are derived using a C-band radar observation operator (Ryzhkov et al., 2011).

3 Results

3.1 Observed Negative K_{DP}

Manual examination of CSAPR2 RHI scans from 413 deep convective cells identifies 238 cases ($\sim$57.6%) in which at least one scan contains a spatially coherent region of negative K_{DP} above the 0°C level. Isolated negative values confined to one or a few radar gates are excluded. To assess the reproducibility of this classification, the RHI scans are independently examined by two coauthors. Our classifications differ for less than 1.7% of the cells, indicating high inter-reviewer consistency. Many of these negative K_{DP} signatures are also evident in the collocated NEXRAD S-band KHGX radar observations (e.g., Fig. S1), re-

ducing the likelihood that these features result solely from a C-band-radar-specific retrieval artifact.

Lightning activity is evaluated using quality-controlled HLMA very-high-frequency (VHF) source locations. HLMA events are considered valid if they have a reduced chi-square value $\chi^2 < 2.0$ and are detected by at least six stations. The reduced χ^2 value measures the normalized timing-residual misfit of the HLMA VHF source-location solution, with values closer to 1 indicating better agreement between observed and fitted station arrival times. This quality-control criterion retains well-constrained lightning source locations and filters out poorly constrained solutions (Thomas et al., 2004). To associate the quality-controlled HLMA sources with individual RHI scans, sources are required to occur within ±30 s of the scan time and within 1° of the RHI azimuth. A cell is classified as lightning active when at least one valid HLMA source satisfies these temporal and azimuthal criteria during CSAPR2 sampling interval. Based on this definition, 123 of the 413 cells (∼29.8%) are classified as lightning active. This percentage represents a lower-bound estimate because HLMA observations are unavailable for 47 convective cells sampled during 26–30 June 2022. The larger number of negative-K_{DP} cases (238) than lightning-active cases (123) indicates that negative K_{DP} was not always accompanied by lightning detected by HLMA during the sampled RHI scans. This discrepancy may arise from the portion of the convective-cell life cycle sampled by CSAPR2, the limited two-dimensional spatial sampling of the RHI scans, or variations in HLMA detection efficiency and station geometry. Alternatively, some cells may have contained in-cloud electric fields strong enough to modify the canting-angle distribution of ice particles but below the threshold required to initiate detectable lightning.

Among the 123 lightning-active cases, 49 cases (∼39.8%) exhibit negative K_{DP} above the melting layer together with lightning activity near the negative K_{DP} region. These cases include both simultaneous occurrence within the same RHI scan and short lead-lag relationships, in which negative K_{DP} precedes lightning activity or lightning activity precedes enhanced negative K_{DP} over one or more RHI scan intervals. This count should be interpreted as a conservative subset of the lightning-active cases, because spatial proximity and/or temporal consistency between lightning and the negative K_{DP} region are required. If only simple co-occurrence is considered, where negative K_{DP} and lightning activity occur anywhere within the same cell without requiring spatial or temporal correspondence, the number of overlapping cases would be larger. Because the RHI scans provide only intermittent two-dimensional slices through evolving three-dimensional convective cells, the spatial and temporal relationship between negative K_{DP} regions and lightning activity needs to be examined on a case-by-case basis. A representative case from August 24, 2022 is shown in Fig. 1. The K_{DP} fields shown in Figs. 1c1–c4 are estimated using the current U.S. National Weather Service (NWS) operational algorithm (Ryzhkov et al., 2005; Reimel & Kumjian, 2021). These estimates are consistent in magnitude and spatial patterns with those in the CSAPR2 optimized convective-cell-tracking dataset (Oue et al., 2023), where K_{DP} is estimated using both the technique of Hubbert and Bringi (1995) and its updated version in the Lidar Radar Open Software Environment (LROSE) (Fig. S1).

In this convective cell observed by CSAPR2 between 08:09:45–08:15:41 UTC, the Z_{H} fields indicate a persistent deep convective echo extending above the −50°C level, with the strongest reflectivity located in the low-level core region below the 0°C level (Figs. 1a1–a4). The corresponding Z_{DR} fields show positive values mainly below and near the 0°C level, consistent with liquid or melting hydrometeors, while reduced or negative Z_{DR} appears in the upper mixed-phase and glaciated regions above the 0°C level (Figs. 1b1–b4). In the K_{DP} field at 08:09:45 UTC, positive values are mainly confined to the lower part (below the −10°C level) of the convective cell, whereas pronounced negative K_{DP} values $< -1\ ^\circ\,\mathrm{km}^{-1}$ appear above the −20°C level (Fig. 1c1). About 2 min later (08:11:42 UTC), HLMA sources are observed and concentrated near the same upper-level negative K_{DP} region while the magnitude of negative K_{DP} decreased (Fig. 1c2). This sequence then repeated during the cell

evolution, with newly formed negative K_{DP} followed by subsequent lightning enhancement (Figs. 1c3–c4).

The coherent negative Z_{DR} signatures, particularly those in Figs. 1b3–b4, broadly coincide with the negative K_{DP} regions in Figs. 1c3–c4 and cannot be attributed solely to masking by near-isometric graupel or aggregates. This collocation is consistent with a population of anisotropic ice particles having a net vertical or canted orientation. Because CSAPR2 employs simultaneous H/V transmission, however, cross-coupling associated with aligned ice crystals may also influence the magnitude and sign of the measured Z_{DR}. Accordingly, negative Z_{DR} is treated here as supporting evidence for electrical alignment rather than as a unique indicator of particle habit.

Manual examination indicates that 28 of the 49 cases ($\sim$57.1%) exhibit a similar sequence, in which negative K_{DP} signatures above the 0°C level are followed by enhanced lightning activity (not shown). This behavior suggests a close relationship between the evolution of electrified ice microphysics and lightning activity: small ice crystals electrically aligned by the ambient electric field, observed as negative K_{DP}, may relax toward their default near-horizontal aerodynamic orientation after lightning discharges weaken the local electric field. Such electric-field-induced ice-crystal alignment and its response to lightning discharges have been documented in previous studies (e.g., Hendry & McCormick, 1976; Weinheimer & Few, 1987; Metcalf, 1995; Krehbiel et al., 1996; Metcalf, 1997; Saunders & Rimmer, 1999; Foster & Hallett, 2002). In the next section, high-resolution LES simulations and sensitivity experiments are used to examine how SIP processes contribute to the development of these negative K_{DP} signatures above the melting layer.

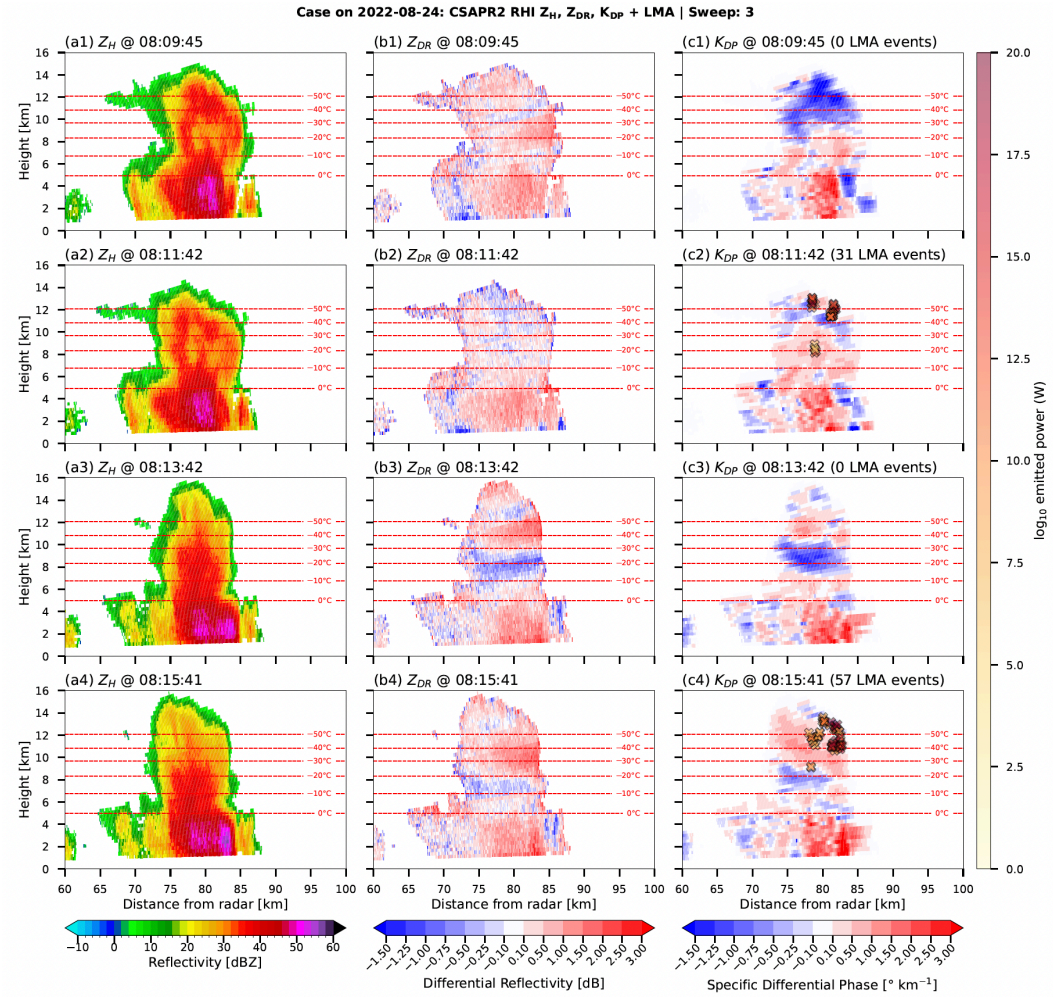

Figure 1. CSAPR2 RHI observations for the 24 August 2022 case, showing the evolution of storm structure and lightning activity from 08:09:45 to 08:15:41 UTC. Columns show (a1–a4) horizontal reflectivity (Z_{H}, in dBZ), (b1–b4) differential reflectivity (Z_{DR}, in dB), and (c1–c4) specific differential phase (K_{DP}, in $^\circ\,\mathrm{km}^{-1}$). HLMA sources are overlaid on the K_{DP} panels where present, with marker color indicating $\log_{10}$ emitted power in W; event counts are given in each panel title. Red dashed lines denote ERA5 environmental isotherms from 0 to −50°C at 10°C intervals.

3.2 Simulated Negative K_{DP}

To examine whether numerical models can reproduce the observed negative-K_{DP} region above the melting layer, and to evaluate the role of SIP processes in producing this polarimetric signature, LES simulations and sensitivity experiments described above are conducted for the representative isolated deep convection case on 24 August 2022 (Fig. 1). Thermodynamic and kinematic profiles for this case (Fig. S2) are extracted from the nearest ERA5 grid point at 0700 UTC on 24 August 2022, about one hour before convection initiation, and are used as the model input sounding. The sounding features a near-surface inversion and a surface-based convective available potential energy of 1793 J kg^{-1} (Fig. S2). The prescribed aerosol size distribution is represented by three lognormal modes, with total number concentrations of 818.5, 660.0, and 380.0 cm^{-3}; median diameters of 23.7, 57.0, and 170.0 nm; and geometric standard deviations of 1.578, 1.420, and 1.477, respectively (Fig. S3). These parameters are derived from mean scanning mobility particle sizer (SMPS) observations (Kuang et al., 2024) collected between 0600 and 0700 UTC on 24 August 2022 during the TRACER field campaign. The vertical aerosol profile is specified using the vertical scaling factor from the TRACER Model Intercomparison Project (MIP) (Fan et al., 2024).

The simulations with (SIPsOn) and without (SIPsOff) SIP reproduce the observed deep convective structure, with similar echo-top heights of ∼16 km compared with the CSAPR2 RHI observations (Fig. S4). However, the simulated Z_H is generally stronger than observed, especially in the lower to middle troposphere (below the −20°C level). In particular, the simulated 50–60-dBZ core extends to ∼7–8 km, whereas observed Z_H exceeding 50 dBZ is mainly confined below ∼5 km. Similarly, simulated reflectivity exceeding 40 dBZ extends to ∼14 km, compared with ∼12 km in the observations. These differences indicate a vertical over-extension of high Z_H by ∼2–3 km, primarily associated with excessive simulated large hail above the freezing level and large raindrops below it (not shown). A future implementation of the hail-melting scheme proposed by Ryzhkov et al. (2013) may help reduce this bias. Compared with SIPsOff, SIPsOn lowers the upper extent of the $Z_H \geq 50$ dBZ core by ∼1 km and slightly reduces its horizontal coverage (Fig. S4). This reduction suggests that SIP redistributes condensate from large precipitating particles toward smaller ice particles, thereby reducing the positive Z_H bias. Nevertheless, a substantial bias remains, with the simulated high-Z_H core extending ∼2 km higher than observed. To further examine the relative contributions of ice-particle production processes in convection, we calculate the fractional contribution of each ice-production process to the total ice particle number production rate along a cross section through the convective cell (Fig. 2). Within the mixed-phase updraft core above the freezing level ($x =$ ∼50–55 km, height between ∼6–9 km), FFD dominates ice particle number production, with the largest production rates concentrated near ∼−10°C (∼7 km height), which is outside the typical temperature range for HM (−3 to −8°C). Outside the liquid-rich updraft region, primary ice production (PIP) becomes the major contributor, especially in the colder cloud region between about −20 and −40°C (∼9–11 km height). These results suggest that the simulated enhancement of ice number concentration in the convective cell is mainly controlled by FFD in the active mixed-phase updraft, while PIP dominates in colder regions where supercooled liquid water is limited (less than 0.01 g m^{-3}).

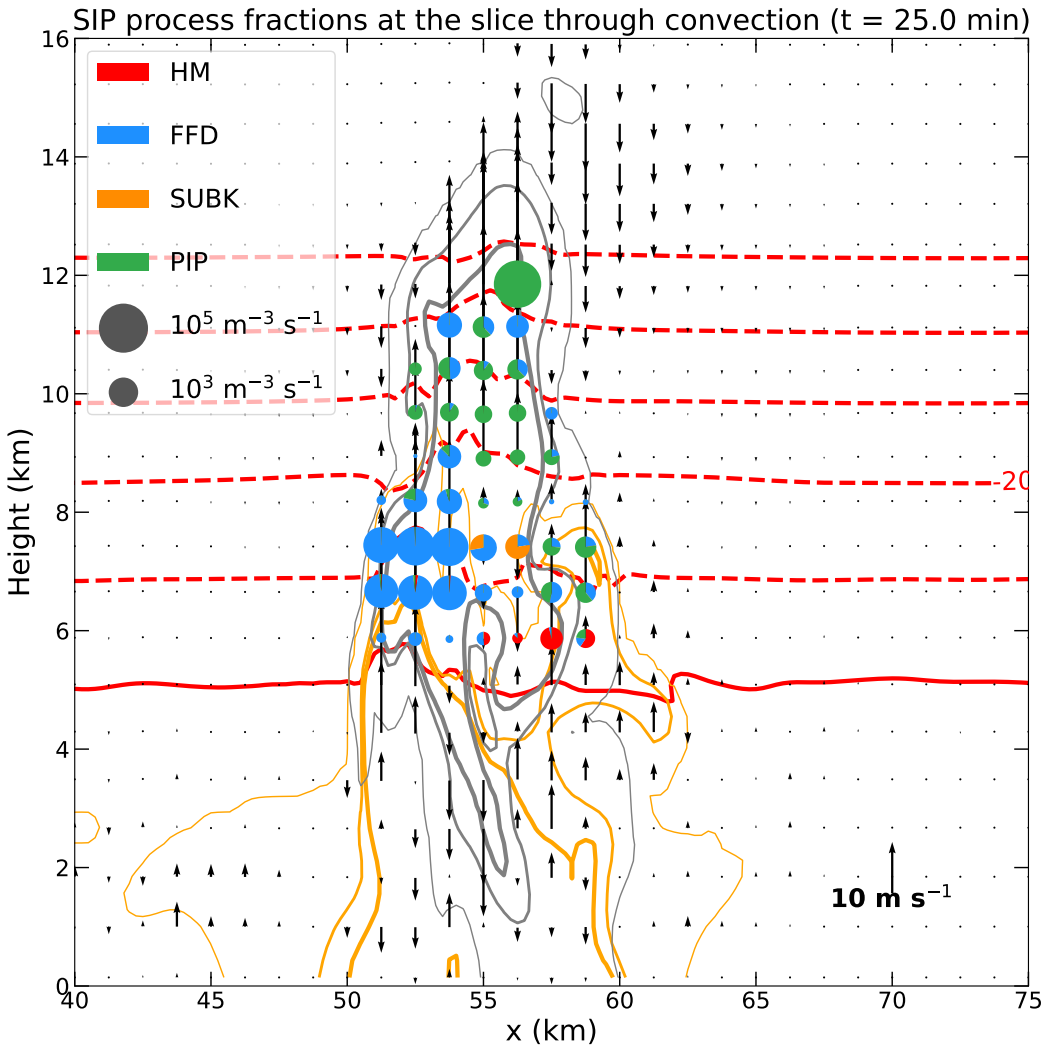

Figure 2. Vertical cross section through the simulated convective cell at $t = 25$ min in the SIPsOn experiment, showing the fractional contributions of ice-particle production processes to the ice particle number production rate. Processes include primary ice production (PIP; green), including both homogeneous and heterogeneous ice nucleation, and secondary ice production by HM (red), FFD (blue), and SUBK (orange). Marker size indicates the total ice particle number production rate. Gray and orange contours show ice water content (IWC) and liquid water content (LWC), respectively, at 0.01, 1.0, and 2.0 g m^{-3}. Red contours denote temperature isotherms from 0 to -50°C at 10°C intervals. Vectors show vertical velocity, with the reference vector corresponding to 10 m s^{-1}.

To examine K_{DP} across all sensitivity experiments, K_{DP} is calculated using the C-band dual-polarization radar simulator of Ryzhkov et al. (2011). In the FSBM scheme, ice particles are represented by two size distributions to reduce computational cost: one for low-density ice particles, including ice crystals ($D \leq 263.22$ μm) and snow ($D > 263.22$ μm), and one for high-density particles, such as hail in this study (Shpund et al., 2019). Weinheimer and Few (1987) calculated electrical and aerodynamic torques for thunderstorm ice particles and showed that, for electric fields of order 100 kV m^{-1}, electric-field alignment can occur for crystals with major dimensions from roughly 200 μm to 1 mm, depending on particle habit. The FSBM scheme used in this study does not include parameterizations of charging and discharging processes and therefore cannot explicitly simulate in-cloud electric fields. To evaluate the proposed mechanism within this limitation, small ice particles ($D \leq 263.22$ μm, corresponding to the size threshold for ice crystals in FSBM) are assumed to be vertically oriented in the radar simulator as a sensitivity-test framework.

Figure 3 decomposes the simulated K_{DP} field into hydrometeor contributions to identify the processes responsible for negative K_{DP} above the melting layer. In all experiments, drops produce strong positive K_{DP} below and near the melting layer (Figs. 3a1–e1), whereas the hail contribution is relatively weak and mostly positive (Figs. 3a3–e3). In contrast, pronounced negative K_{DP} ($< -0.5^{\circ}$ km^{-1}) appears in the snow contribution only when FFD is included, as shown in the FFDOn and SIPsOn experiments (Figs. 3c2 and e2, c4 and e4). This negative snow K_{DP} signal extends through the upper mixed-phase and glaciated regions (above 7.5 km), where small ice particles are assumed to be vertically oriented in the radar simulator. In FFDOn and SIPsOn, negative K_{DP} extends to altitudes of up to 16 km (Figs. 3c2 and e2, c4 and e4), whereas the observed signature is mainly confined below 15 km (Figs. 1c1–c4). This vertical-extent bias may result from stronger simulated updrafts or the simplified ice-particle orientation assumption used in the radar simulator. Quantifying the contributions of these factors is beyond the scope of this study and will be examined in future work. The absence of comparable negative K_{DP} in SIPsOff, HMOn, and SUBKOn indicates that HM and SUBK alone are insufficient to reproduce the observed upper-level negative K_{DP} signatures.

For this simulated case, these results suggest that SIP processes, especially FFD, are essential for producing enhanced concentrations of small ice particles and for reproducing negative K_{DP} features above the melting layer. However, simulated negative K_{DP} magnitudes below $\sim$13 km in FFDOn and SIPsOn (Figs. 3c2 and e2, c4 and e4) remain weaker than observed (Figs. 1c1 and c3). This underestimation may partly reflect the omission of fragmentation during ice–ice collisions, which could provide an additional local source of small ice particles. The restrictive orientation assumption, under which only particles with $D \leq 263.22$ μm are prescribed to be vertically aligned, together with partial cancellation by the weakly positive hail contribution, may further weaken the simulated negative K_{DP} signal.

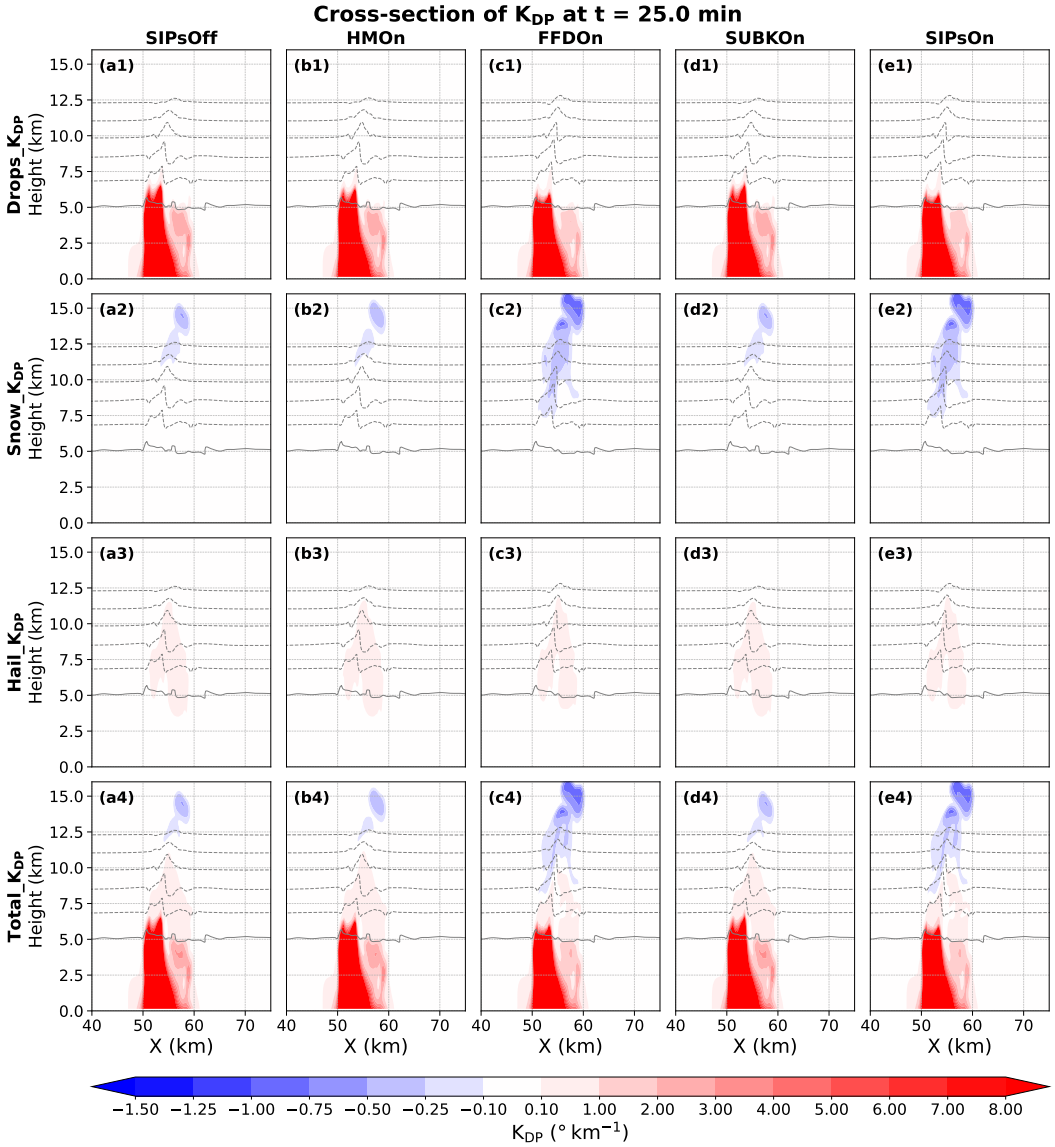

Figure 3. Simulated cross sections of hydrometeor-specific and total specific differential phase (K_{DP}; ° km^{-1}) through the convective cell at $t = 25$ min for the (a1–a4) SIPsOff, (b1–b4) HMOn, (c1–c4) FFDOn, (d1–d4) SUBKOn, and (e1–e4) SIPsOn experiments. Rows show the contributions from drops, snow (including small ice crystals), hail, and total K_{DP}. Gray contours denote temperature isotherms from 0 to −50°C at 10°C intervals. The radar simulator assumes vertically oriented small ice particles ($D \leq 263.22$ μm).

3.3 SIP Impacts on Convective Clouds

To further examine how SIP processes influence convective cloud evolution, Fig. 4 shows time series of ice water path (IWP), liquid water path (LWP), total water path (TWP), and mean accumulated precipitation for the SIP sensitivity experiments of the 24 August 2022 case. Figure 4 shows that SIP processes can modify the simulated bulk water budget and precipitation efficiency of the simulated convective cell. All experiments exhibit rapid cloud development during the first ∼30 min, with peak IWP of ∼0.12–0.15 kg m^{-2} (Fig. 4a), peak LWP of ∼0.18–0.20 kg m^{-2} (Fig. 4b), and peak TWP of ∼0.27 kg m^{-2} (Fig. 4c). After this developing stage, the experiments including FFD, i.e., FFDOn and SIPsOn, maintain larger IWP, with values remaining near 0.04–0.05 kg m^{-2} by 120 min, compared with ∼0.02 kg m^{-2} in SIPsOff, HMOn, and SUBKOn (Fig. 4a). In contrast, LWP decreases more rapidly after its peak and becomes very small (less than 0.01 kg m^{-2}) after ∼60 min in all experiments, with slightly lower values (less than 0.001 kg m^{-2}) when FFD process is included (Fig. 4b). The enhanced IWP and TWP, together with reduced LWP, indicate that FFD shifts condensate from liquid water toward ice-phase particles and helps maintain more condensate in the cloud column, with TWP increasing by up to ∼107% during the later stage. HMOn and SUBKOn remain closer to SIPsOff (Figs. 4a–c), indicating that HM and SUBK have much smaller impacts on the bulk water budget than FFD. The mean accumulated precipitation reaches a quasi-steady value after ∼60 min, by which time the storm has completely dissipated. Both SIPsOn and FFDOn produce less accumulated precipitation than SIPsOff, with a reduction of ∼7.6% in SIPsOn relative to SIPsOff (Fig. 4d). Therefore, these results suggest that FFD is the SIP pathway most responsible for shifting condensate from liquid water toward ice-phase particles and for reducing warm-rain or melting-related precipitation efficiency in this simulated convective cell. The weaker responses in HMOn and SUBKOn suggest that these processes alone have limited impact on the domain-integrated water budget compared with FFD.

To further explain the changes in the bulk water budget shown in Fig. 4, vertical profiles of hydrometeor water content (Fig. S5) and major microphysical process rates (Fig. S6) are compared between SIPsOn and SIPsOff. Compared with SIPsOff, SIPsOn produces more cloud ice ($D \leq 263.22$ μm) in the upper mixed-phase and glaciated regions above the −10°C level at t = 20–40 min, while cloud water ($D < 101.59$ μm), rain ($D \geq 101.59$ μm), snow ($D > 263.22$ μm), and hail water contents are generally reduced or remain comparable after the developing stage (t = 30–40 min; Fig. S5). This indicates that the larger IWP in SIPsOn is mainly associated with enhanced small-ice mass rather than increased precipitation-sized hydrometeors. The reduced rain and hail water contents are also consistent with the smaller accumulated precipitation in SIPsOn. During the active convective stage (t = 20–30 min), SIPsOn modifies ice-phase growth and sedimentation near and above the melting layer, with enhanced ice/snow depositional growth and reduced conversion toward large sedimenting hail compared with SIPsOff (Fig. S6). These changes suggest that SIP, especially FFD, increases the number of small ice particles, redistributes condensate from liquid water and large precipitating particles toward cloud ice ($D \leq 263.22$ μm), and reduces precipitation efficiency. Therefore, the larger IWP, lower LWP, and ∼7.6% reduction in accumulated precipitation in SIPsOn are physically consistent with a microphysical shift toward smaller ice particles and weaker production or fallout of large precipitation-sized hydrometeors.

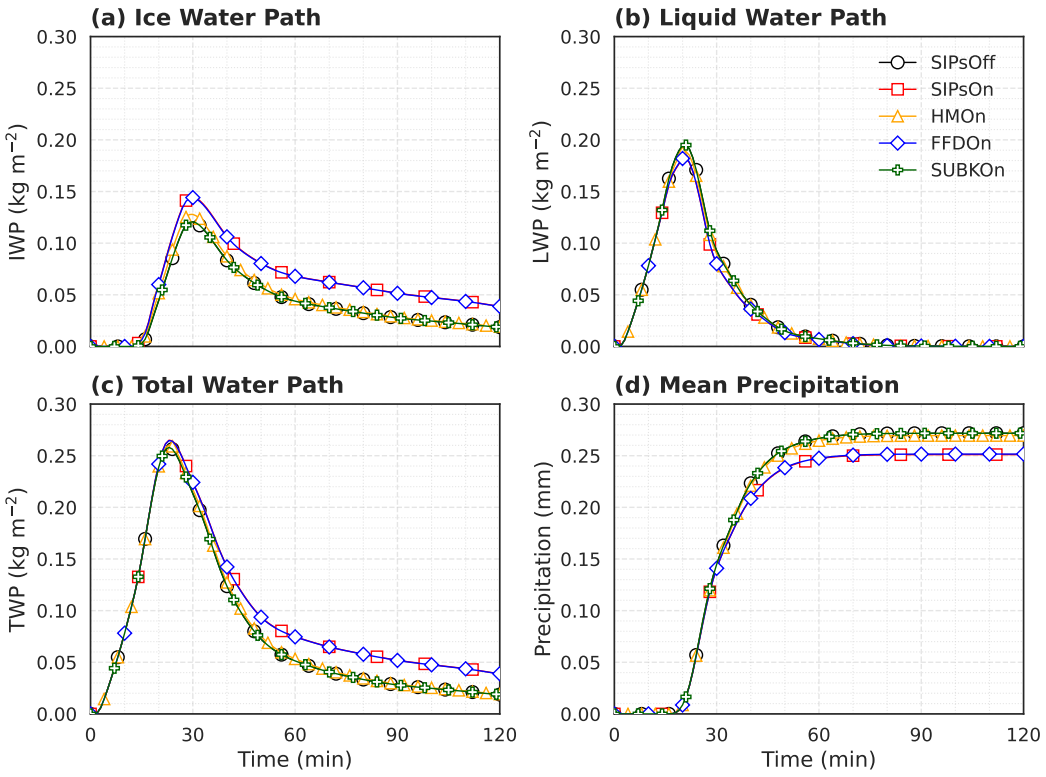

Figure 4. Time series of (a) ice water path (IWP, in kg m^{-2}), (b) liquid water path (LWP, in kg m^{-2}), (c) total water path (TWP, in kg m^{-2}), and (d) mean accumulated precipitation (mm) for the SIP sensitivity experiments, including SIPsOff, SIPsOn, HMOn, FFDOn, and SUBKOn.

4 Summary and Conclusions

In this study, TRACER radar observations, lightning observations, and WRF-LES sensitivity simulations are used to investigate the occurrence of negative K_{DP} above the melting layer in deep convective clouds and to evaluate its possible microphysical origin. The major findings are summarized as follows:

1. Negative K_{DP} regions are frequently identified above the melting layer in convective clouds. These signatures are consistently detected by both TRACER research C-band radar observations and operational S-band radar observations, indicating that the observed negative K_{DP} features are unlikely artifacts of a single radar system or retrieval method.

2. The negative K_{DP} regions are closely associated with lightning activity. The collocation between negative K_{DP} and HLMA sources suggests that these signatures are related to active mixed-phase microphysical and electrification processes. This relationship, consistent with previous studies, supports the interpretation that the negative K_{DP} signatures are associated with small, vertically oriented, electrically aligned needle- or column-like ice particles in the upper mixed-phase and glaciated regions of deep convection.

3. WRF-LES sensitivity simulations show that negative K_{DP} is reproduced with high likelihood only when SIP processes are included, especially FFD. Including SIP processes shifts the simulated cloud toward larger ice water path, smaller liquid water path, and $\sim$7.6% less accumulated precipitation. These results indicate that SIP processes, particularly FFD, can substantially modify ice particle number concentration, cloud water partitioning, and precipitation production in deep convective clouds.

To the best of our knowledge, this study provides the first combined observational and modeling evidence that negative K_{DP} above the melting layer can serve as a radar signature of electrically aligned ice particles *associated with SIP* and storm electrification. These findings provide constraints for improving the representation of ice microphysical processes in numerical models. Despite several decades of research and the proposal of multiple SIP mechanisms, such as rime splintering, fragmentation of freezing droplets, and ice–ice collision breakup, large uncertainties remain in their quantitative rates, timing, and required environmental conditions in natural cloud systems, and their parameterizations in numerical models. Meanwhile, uncertainties in SIP process rates in numerical models arise not only from SIP parameterizations themselves, but also from the simulated hydrometeor populations produced by other microphysical processes and by different microphysics schemes. These uncertainties can further affect the simulated influence of SIP on surface precipitation, such as the contrasting precipitation responses reported in previous studies (Georgakaki et al., 2022; Han et al., 2024; Calderón et al., 2025; Grzegorczyk, Wobrock, Dziduch, & Planche, 2025; Grzegorczyk, Wobrock, Canzi, et al., 2025b; Sun et al., 2025). Although the synergistic ESCAPE field campaign collected in-situ observations of convective clouds, these measurements were not collocated with the convective cells sampled by CSAPR2 during TRACER. In addition, the ESCAPE research flights were conducted mainly below the -10°C level (Kollias et al., 2025; Huang, McFarquhar, Patil, et al., 2025), generally lower than the regions where negative K_{DP} signatures were observed. Future work should combine in-situ ice particle observations, in-cloud electric field measurements, laboratory experiments, and model developments that explicitly represent charging and discharging processes and better constrain SIP parameterizations using both field observations and laboratory measurements. Implementing such parameterizations in cloud-resolving models will be important for directly simulating in-cloud electric fields and further testing the proposed link among SIP, electrically aligned ice particles, negative K_{DP}, and lightning activity.

Open Research Section

TRACER CSAPR2 optimized convective cell tracking dataset is available at `https://doi.org/10.5439/1969992` (Oue et al., 2023). NEXRAD radar dataset is available at the NOAA AWS S3 bucket (`https://registry.opendata.aws/noaa-nexrad`). The Houston Lightning Mapping Array data are available at `https://doi.org/10.26023/GBKS-E7VT-HS11` (Logan et al., 2023). TRACER SMPS aerosol data are available at `https://doi.org/10.5439/1476898` (Kuang et al., 2024). ERA5 reanalysis dataset is available at `https://doi.org/10.5065/BH6N-5N20` (Hersbach et al., 2020). The WRF code is available at `https://github.com/wrf-model/WRF` (DOI: `https://doi.org/10.5065/D6MK6B4K`).

Conflict of Interest disclosure

The authors declare there are no conflicts of interest for this manuscript.

Acknowledgments

This research was first presented at the 41st International Conference on Radar Meteorology, held in Toronto, Ontario, Canada, 25–29 August 2025 (Huang, McFarquhar, Ryzhkov, et al., 2025). This research was supported primarily by the U.S. Department of Energy (DOE)'s Atmospheric System Research (ASR), an Office of Science Biological and Environmental Research program, under Grant DE-SC0024317 and under Contract DE-SC0012704, and the National Science Foundation (NSF) (Award AGS-2019968), and by the NOAA/Office of Oceanic and Atmospheric Research under NOAA–University of Oklahoma Cooperative Agreement #NA21OAR4320204, U.S. Department of Commerce. The authors thank Edward Mansell and Kristin Calhoun of the NOAA National Severe Storms Laboratory for their constructive internal reviews. The computing for this project was primarily performed at the University of Oklahoma (OU) Supercomputing Center for Education and Research (OSCER).

References

Berdeklis, P., & List, R. (2001). The ice crystal–graupel collision charging mechanism of thunderstorm electrification. *Journal of the atmospheric sciences*, *58*(18), 2751–2770. doi: 10.1175/1520-0469(2001)058<2751:TICGCC>2.0.CO;2

Biggerstaff, M. I., Zounes, Z., Addison Alford, A., Carrie, G. D., Pilkey, J. T., Uman, M. A., & Jordan, D. M. (2017). Flash propagation and inferred charge structure relative to radar-observed ice alignment signatures in a small florida mesoscale convective system. *Geophysical Research Letters*, *44*(15), 8027–8036. doi: 10.1002/2017GL074610

Bruning, E. C., Brunner, K. N., van Lier-Walqui, M., Logan, T., & Matsui, T. (2024). Lightning and radar measures of mixed-phase updraft variability in tracked storms during the tracer field campaign in houston, texas. *Monthly Weather Review*, *152*(12), 2753–2769. doi: 10.1175/MWR-D-24-0060.1

Calderón, S. M., Hyttinen, N., Kokkola, H., Raatikainen, T., Lawson, R. P., & Romakkaniemi, S. (2025). Secondary ice formation in cumulus congestus clouds: insights from observations and aerosol-aware large-eddy simulations. *Atmospheric Chemistry and Physics*, *25*(21), 14479–14500. doi: 10.5194/acp-25-14479-2025

Caylor, I., & Chandrasekar, V. (1996). Time-varying ice crystal orientation in thunderstorms observed with multiparameter radar. *IEEE transactions on geoscience and remote sensing*, *34*(4), 847–858. doi: 10.1109/36.508402

Deshmukh, A., Phillips, V. T., Bansemer, A., Patade, S., & Waman, D. (2022). New empirical formulation for the sublimational breakup of graupel and dendritic snow. *Journal of the Atmospheric Sciences*, *79*(1), 317–336. doi: 10.1175/JAS-D-20-0275.1

Fan, J., Saleeby, S., Jensen, M., van den Heever, S., Kollias, P., Subba, T., … Oue, M. (2024). *Tracking Aerosol Convection Interaction Experiment (TRACER) Model Intercompar-*

ison Project (MIP) Roadmap. Retrieved from `https://arm-synergy.github.io/tracer-mip`

Field, P. R., Lawson, R. P., Brown, P. R., Lloyd, G., Westbrook, C., Moisseev, D., … others (2017). Secondary ice production: Current state of the science and recommendations for the future. *Meteorological Monographs*, *58*, 7–1. doi: 10.1175/AMSMONOGRAPHS-D-16-0014.1

Figueras i Ventura, J., Honore, F., & Tabary, P. (2013). X-band polarimetric weather radar observations of a hailstorm. *Journal of Atmospheric and Oceanic Technology*, *30*(9), 2143–2151. doi: 10.1175/JTECH-D-12-00243.1

Foster, T., & Hallett, J. (2002). The alignment of ice crystals in changing electric fields. *Atmospheric research*, *62*(1-2), 149–169. doi: 10.1016/S0169-8095(02)00008-X

Georgakaki, P., Sotiropoulou, G., Vignon, É., Billault-Roux, A.-C., Berne, A., & Nenes, A. (2022). Secondary ice production processes in wintertime alpine mixed-phase clouds. *Atmospheric Chemistry and Physics*, *22*(3), 1965–1988. doi: 10.5194/acp-22-1965-2022

Grzegorczyk, P., Wobrock, W., Canzi, A., Niquet, L., Tridon, F., & Planche, C. (2025a). Investigating secondary ice production in a deep convective cloud with a 3d bin microphysics model: Part ii-effects on the cloud formation and development. *Atmospheric Research*, *314*, 107797. doi: 10.1016/j.atmosres.2024.107797

Grzegorczyk, P., Wobrock, W., Canzi, A., Niquet, L., Tridon, F., & Planche, C. (2025b). Investigating secondary ice production in a deep convective cloud with a 3d bin microphysics model: Part ii-effects on the cloud formation and development. *Atmospheric Research*, *314*, 107797. doi: 10.1016/j.atmosres.2024.107797

Grzegorczyk, P., Wobrock, W., Dziduch, A., & Planche, C. (2025). Influence of secondary ice production on cloud and rain properties: analysis of the hymex iop7a heavy-precipitation event. *Atmospheric Chemistry and Physics*, *25*(17), 10403–10420. doi: 10.5194/acp-25-10403-2025

Hallett, J., & Mossop, S. (1974). Production of secondary ice particles during the riming process. *Nature*, *249*(5452), 26–28. doi: 10.1038/249026a0

Han, C., Hoose, C., & Dürlich, V. (2024). Secondary ice production in simulated deep convective clouds: A sensitivity study. *Journal of the Atmospheric Sciences*, *81*(5), 903–921. doi: 10.1175/JAS-D-23-0156.1

Hendry, A., & McCormick, G. (1976). Radar observations of the alignment of precipitation particles by electrostatic fields in thunderstorms. *Journal of Geophysical Research*, *81*(30), 5353–5357. doi: 10.1029/JC081i030p05353

Hersbach, H., Bell, B., Berrisford, P., Hirahara, S., Horányi, A., Muñoz-Sabater, J., … others (2020). The era5 global reanalysis. *Quarterly Journal of the Royal Meteorological Society*, *146*(730), 1999–2049. doi: 10.1002/qj.3803

Huang, Y., McFarquhar, G. M., Patil, S. U., Gao, L., Taszarek, M., Xue, M., … others (2025). Dependence of convective cloud microphysical properties on environmental conditions during the tracer and escape field campaigns: A synergistic approach of observations, machine learning, and parcel models. *Journal of the Atmospheric Sciences*, *82*(10), 2291–2312. doi: 10.1175/JAS-D-24-0269.1

Huang, Y., McFarquhar, G. M., Ryzhkov, A. V., Xue, M., Mise, D. J., Snyder, J. C., … Jensen, M. P. (2025). Secondary ice production in deep convective clouds over coastal urban areas: Insights from tracer radar observations and large-eddy simulations. In *41st international conference on radar meteorology.*

Huang, Y., Wu, W., McFarquhar, G. M., Xue, M., Morrison, H., Milbrandt, J., … Heckman, I. (2022). Microphysical processes producing high ice water contents (hiwcs) in tropical convective clouds during the haic-hiwc field campaign: dominant role of secondary ice production. *Atmospheric Chemistry and Physics*, *22*, 2365–2384. Retrieved from `https://doi.org/10.5194/acp-22-2365-2022` doi: 10.5194/acp-22-2365-2022

Hubbert, J., & Bringi, V. (1995). An iterative filtering technique for the analysis of copolar differential phase and dual-frequency radar measurements. *Journal of Atmospheric and Oceanic Technology*, *12*(3), 643–648. doi: 10.1175/1520-0426(1995)012<0643:

AIFTFT>2.0.CO;2

Hubbert, J., Ellis, S., Chang, W.-Y., Rutledge, S., & Dixon, M. (2014). Modeling and interpretation of s-band ice crystal depolarization signatures from data obtained by simultaneously transmitting horizontally and vertically polarized fields. *Journal of Applied Meteorology and Climatology*, *53*(6), 1659–1677. doi: 10.1175/JAMC-D-13-0158.1

Jeevanjee, N. (2017). Vertical velocity in the gray zone. *Journal of Advances in Modeling Earth Systems*, *9*(6), 2304–2316. doi: 10.1002/2017MS001059

Jensen, M. P., Flynn, J. H., Gonzalez-Cruz, J. E., Judd, L. M., Kollias, P., Kuang, C., … others (2025). Studying aerosol, clouds, and air quality in the coastal urban environment of southeastern texas. *Bulletin of the American Meteorological Society*, BAMS–D. doi: 10.1175/BAMS-D-23-0331.1

Kollias, P., Luke, E., Oue, M., & Lamer, K. (2020). Agile adaptive radar sampling of fast-evolving atmospheric phenomena guided by satellite imagery and surface cameras. *Geophysical Research Letters*, *47*(14), e2020GL088440. doi: 10.1029/2020GL088440

Kollias, P., McFarquhar, G. M., Bruning, E., DeMott, P. J., Kumjian, M. R., Lawson, P., … others (2025). Experiment of sea breeze convection, aerosols, precipitation, and environment (escape). *Bulletin of the American Meteorological Society*, *106*(2), E310–E332. doi: 10.1175/BAMS-D-23-0014.1

Korolev, A., & Leisner, T. (2020). Review of experimental studies of secondary ice production. *Atmospheric Chemistry and Physics*, *20*(20), 11767–11797. doi: 10.5194/acp-20-11767-2020

Korolev, A., Qu, Z., Milbrandt, J., Heckman, I., Cholette, M., Wolde, M., … Fridlind, A. M. (2024). High ice water content in tropical mesoscale convective systems (a conceptual model). *Atmospheric Chemistry and Physics*, *24*(20), 11849–11881. doi: 10.5194/acp-24-11849-2024

Krehbiel, P., Chen, T., McCrary, S., Rison, W., Gray, G., & Brook, M. (1996). The use of dual channel circular-polarization radar observations for remotely sensing storm electrification. *Meteorology and Atmospheric Physics*, *59*(1), 65–82. doi: 10.1007/BF01032001

Kuang, C., Singh, A., Howie, J., Salwen, C., & Hayes, C. (2024). *Scanning Mobility Particle Sizer (AOSSMPS).* ARM Data Center. (Dataset accessed 2024-09-27) doi: 10.5439/1476898

Lawson, R. P., Bruintjes, R., Woods, S., & Gurganus, C. (2022). Coalescence and secondary ice development in cumulus congestus clouds. *Journal of the Atmospheric Sciences*, *79*(4), 953–972. doi: 10.1175/JAS-D-21-0188.1

Lawson, R. P., Korolev, A. V., DeMott, P. J., Heymsfield, A. J., Bruintjes, R. T., Wolff, C. A., … others (2023). The secondary production of ice in cumulus experiment (spicule). *Bulletin of the American Meteorological Society*, *104*(1), E51–E76. doi: 10.1175/BAMS-D-21-0209.1

Lawson, R. P., Woods, S., & Morrison, H. (2015). The microphysics of ice and precipitation development in tropical cumulus clouds. *Journal of the Atmospheric Sciences*, *72*(6), 2429–2445. doi: 10.1175/JAS-D-14-0274.1

Logan, T., Bruning, E., Brunner, K., & Souza, J. (2023). *Houston Lightning Mapping Array (HLMA) Flash-level data. Version 1.0.* UCAR/NCAR-Earth Observing Laboratory. doi: 10.26023/GBKS-E7VT-HS11

Mattos, E. V., Machado, L. A., Williams, E. R., & Albrecht, R. I. (2016). Polarimetric radar characteristics of storms with and without lightning activity. *Journal of Geophysical Research: Atmospheres*, *121*(23), 14–201. doi: 10.1002/2016JD025142

Mattos, E. V., Machado, L. A., Williams, E. R., Goodman, S. J., Blakeslee, R. J., & Bailey, J. C. (2017). Electrification life cycle of incipient thunderstorms. *Journal of Geophysical Research: Atmospheres*, *122*(8), 4670–4697. doi: 10.1002/2016JD025772

Metcalf, J. I. (1995). Radar observations of changing orientations of hydrometeors in thunderstorms. *Journal of Applied Meteorology and Climatology*, *34*(4), 757–772. doi: 10.1175/1520-0450(1995)034<0757:ROOCOO>2.0.CO;2

Metcalf, J. I. (1997). Temporal and spatial variations of hydrometeor orientations in thunderstorms. *Journal of Applied Meteorology*, *36*(4), 315–321. doi: 10.1175/1520-0450(1997)036<0315:TASVOH>2.0.CO;2

Mise, D. J., Huang, Y., McFarquhar, G. M., Xue, M., Ryzhkov, A. V., Snyder, J., … Taszarek, M. (2026). Dependence of Convective Cell Properties on Meteorological and Aerosol Conditions during TRACER. *Journal of the Atmospheric Sciences*. doi: 10.1175/JAS-D-25-0130.1

Oue, M., Treserras, B. P., Luke, E. P., & Kollias, P. (2023). *CSAPR2 Optimized Convective Cell Tracking Data During TRACER* (Tech. Rep.). Oak Ridge National Laboratory (ORNL), Oak Ridge, TN (United States). doi: 10.2172/2007152

Patil, S., McFarquhar, G. M., Huang, Y., Roberts, G., Wolde, M., Nichman, L., … others (2026). Quasi-steady state supersaturation: Do high values derived from escape represent real high supersaturations and the potential for condensational invigoration? *Journal of Geophysical Research: Atmospheres*, *131*(12), e2025JD045547. doi: 10.1029/2025JD045547

Phillips, V. T., Formenton, M., Kanawade, V. P., Karlsson, L. R., Patade, S., Sun, J., … others (2020). Multiple environmental influences on the lightning of cold-based continental cumulonimbus clouds. part i: Description and validation of model. *Journal of the Atmospheric Sciences*, *77*(12), 3999–4024. doi: 10.1175/JAS-D-19-0200.1

Phillips, V. T., Patade, S., Gutierrez, J., & Bansemer, A. (2018). Secondary ice production by fragmentation of freezing drops: Formulation and theory. *Journal of the Atmospheric Sciences*, *75*(9), 3031–3070. doi: 10.1175/JAS-D-17-0190.1

Qu, Z., Korolev, A., Milbrandt, J. A., Heckman, I., Huang, Y., McFarquhar, G. M., … Nguyen, C. (2022). The impacts of secondary ice production on microphysics and dynamics in tropical convection. *Atmospheric Chemistry and Physics*, *22*(18), 12287–12310. doi: 10.5194/acp-22-12287-2022

Reimel, K. J., & Kumjian, M. (2021). Evaluation of k dp estimation algorithm performance in rain using a known-truth framework. *Journal of Atmospheric and Oceanic Technology*, *38*(3), 587–605. doi: 10.1175/JTECH-D-20-0060.1

Reynolds, S., Brook, M., & Gourley, M. F. (1957). Thunderstorm charge separation. *Journal of Atmospheric Sciences*, *14*(5), 426–436. doi: 10.1175/1520-0469(1957)014<0426:TCS>2.0.CO;2

Ryzhkov, A. V., Kumjian, M. R., Ganson, S. M., & Khain, A. P. (2013). Polarimetric radar characteristics of melting hail. part i: Theoretical simulations using spectral microphysical modeling. *Journal of Applied Meteorology and Climatology*, *52*(12), 2849–2870. doi: 10.1175/JAMC-D-13-073.1

Ryzhkov, A. V., Pinsky, M., Pokrovsky, A., & Khain, A. (2011). Polarimetric radar observation operator for a cloud model with spectral microphysics. *Journal of Applied Meteorology and Climatology*, *50*(4), 873–894. doi: 10.1175/2010JAMC2363.1

Ryzhkov, A. V., Schuur, T. J., Burgess, D. W., Heinselman, P. L., Giangrande, S. E., & Zrnic, D. S. (2005). The joint polarization experiment: Polarimetric rainfall measurements and hydrometeor classification. *Bulletin of the American Meteorological Society*, *86*(6), 809–824. doi: 10.1175/BAMS-86-6-809

Ryzhkov, A. V., & Zrnić, D. S. (2007). Depolarization in ice crystals and its effect on radar polarimetric measurements. *Journal of atmospheric and oceanic technology*, *24*(7), 1256–1267. doi: 10.1175/JTECH2034.1

Ryzhkov, A. V., & Zrnić, D. S. (2019). *Radar polarimetry for weather observations* (Vol. 486). Springer. doi: 10.1007/978-3-030-05093-1

Saunders, C. (2008). Charge separation mechanisms in clouds. *Space Science Reviews*, *137*. doi: 10.1007/s11214-008-9345-0

Saunders, C., Bax-Norman, H., Emersic, C., Avila, E., & Castellano, N. (2006). Laboratory studies of the effect of cloud conditions on graupel/crystal charge transfer in thunderstorm electrification. *Quarterly Journal of the Royal Meteorological Society: A journal of the atmospheric sciences, applied meteorology and physical oceanography*, *132*(621), 2653–2673. doi: 10.1256/qj.05.218

Saunders, C., & Rimmer, J. (1999). The electric field alignment of ice crystals in thunderstorms. *Atmospheric research*, *51*(3-4), 337–343. doi: 10.1016/S0169-8095(99)00018-6

Shpund, J., Khain, A., Lynn, B., Fan, J., Han, B., Ryzhkov, A., … Gill, D. (2019). Simulating a mesoscale convective system using wrf with a new spectral bin microphysics: 1: Hail vs graupel. *Journal of Geophysical Research: Atmospheres*, *124*(24), 14072–14101. doi: 10.1029/2019JD030576

Sun, M., Connolly, P. J., Field, P. R., Finney, D. L., & Blyth, A. M. (2025). Influence of secondary ice formation on tropical deep convective clouds simulated by the unified model. *Atmospheric Chemistry and Physics*, *25*(24), 18549–18569. doi: 10.5194/acp-25-18549-2025

Takahashi, T. (1978). Riming electrification as a charge generation mechanism in thunderstorms. *Journal of Atmospheric Sciences*, *35*(8), 1536–1548. doi: 10.1175/1520-0469(1978)035<1536:REAACG>2.0.CO;2

Thomas, R. J., Krehbiel, P. R., Rison, W., Hunyady, S. J., Winn, W. P., Hamlin, T., & Harlin, J. (2004). Accuracy of the lightning mapping array. *Journal of Geophysical Research: Atmospheres*, *109*(D14). doi: 10.1029/2004JD004549

Vongpaseut, I., & Barthe, C. (2025). Distinct effects of several ice production processes on thunderstorm electrification and lightning activity. *Atmospheric Chemistry and Physics*, *25*(21), 14945–14965. doi: 10.5194/acp-25-14945-2025

Wang, S., Wada, Y., Hayashi, S., Ushio, T., & Chandrasekar, V. (2024a). Electrical alignment signatures of ice particles before intracloud lightning activity detected by dual-polarized phased array weather radar. *Journal of Geophysical Research: Atmospheres*, *129*(7), e2023JD039942. doi: 10.1029/2023JD039942

Wang, S., Wada, Y., Hayashi, S., Ushio, T., & Chandrasekar, V. (2024b, October). Observation of Electrical Alignment Signatures in an Isolated Thunderstorm by Dual-Polarized Phased Array Weather Radar and the Relationship With Intracloud Lightning Flash Rate. *Journal of Geophysical Research: Atmospheres*, *129*(19), e2023JD040681. Retrieved 2025-03-24, from `https://agupubs.onlinelibrary.wiley.com/doi/10.1029/2023JD040681` doi: 10.1029/2023JD040681

Weber, M., Zrnic, D., Zhang, P., & Mansell, E. (2024). Ice crystal alignment: A concept for high-temporal-resolution monitoring using polarimetric phased array radar. *Journal of Applied Meteorology and Climatology*, *63*(3), 455–469. doi: 10.1175/JAMC-D-23-0028.1

Weinheimer, A. J., & Few, A. A. (1987). The electric field alignment of ice particles in thunderstorms. *Journal of Geophysical Research: Atmospheres*, *92*(D12), 14833–14844. doi: 10.1029/JD092iD12p14833

Zrnic, D. S., & Ryzhkov, A. V. (1999). Polarimetry for weather surveillance radars. *Bulletin of the American Meteorological Society*, *80*(3), 389–406. doi: 10.1175/1520-0477(1999)080<0389:PFWSR>2.0.CO;2